Computerized Medical Imaging and Graphics 51 (2016) 1–10

Contents lists available at ScienceDirect

Computerized Medical Imaging and Graphics

journal homepage: www.elsevier.com/locate/compmedimag

Quantitative normal thoracic anatomy at CT

Monica M.S. Matsumoto, Jayaram K. Udupa*, Yubing Tong, Babak Saboury, Drew A. Torigian

Medical Image Processing Group, Department of Radiology, Hospital of the University of Pennsylvania, Philadelphia, United States

ARTICLE INFO

Article history:
Received 7 July 2015
Received in revised form 22 March 2016
Accepted 29 March 2016

Keywords:
Thorax
CT
Quantification
Quantitative radiology
Automatic anatomy recognition
Segmentation

ABSTRACT

Automatic anatomy recognition (AAR) methodologies for a body region require detailed understanding of the morphology, architecture, and geographical layout of the organs within the body region. The aim of this paper was to quantitatively characterize the normal anatomy of the thoracic region for AAR. Contrast-enhanced chest CT images from 41 normal male subjects, each with 11 segmented objects, were considered in this study. The individual objects were quantitatively characterized in terms of their linear size, surface area, volume, shape, CT attenuation properties, inter-object distances, size and shape correlations, size-to-distance correlations, and distance-to-distance correlations. A heat map visualization approach was used for intuitively portraying the associations between parameters. Numerous new observations about object geography and relationships were made. Some objects, such as the pericardial region, vary far less than others in size across subjects. Distance relationships are more consistent when involving an object such as trachea and bronchi than other objects. Considering the inter-object distance, some objects have a more prominent correlation, such as trachea and bronchi, right and left lungs, arterial system, and esophagus. The proposed method provides new, objective, and usable knowledge about anatomy whose utility in building body-wide models toward AAR has been demonstrated in other studies.

© 2016 Elsevier Ltd. All rights reserved.

1. Introduction

The detection of abnormalities on any imaging examination is made possible by first having a thorough knowledge of the normal anatomy and/or function of an organ system under study (i.e., an understanding of what is considered to be normal), and then by characterizing deviations from this normal. In clinical practice, radiological examinations are typically performed in a descriptive and qualitative manner. Although this approach may be useful to describe pertinent findings and to provide an overview of a patient's status, it is imprecise, subjective, and insensitive to small deviations from normal. Quantifiable information can be extracted from available images to optimize early disease detection, accurate disease characterization, and response assessment in the clinical setting, indicating a potential role for quantitative radiology in clinical practice.

Since manual quantitative analysis is labor-intensive and subject to inter-operator variability, computerized *automatic anatomy recognition* (AAR), which we define as automatic modeling identification, and delineation of all major anatomic objects in a body region, is an essential step towards quantitative radiology (Udupa et al., 2014). Its implementation for radiological images in a body-region- and modality-independent manner is, however, challenging. Many investigations are currently underway toward building AAR methodologies. Two separate approaches—atlas-based (Cabezas et al., 2011; Joshi et al., 2004; Baiker et al., 2010; Jia et al., 2012; Evans et al., 2012) and model-based (Cootes et al., 1995; Chen et al., 2013; Chen and Bagci, 2011; Okada et al., 2008; Zhou and Rajapakse, 2005) are the most prominent among these. Motivated by applications (such as semantic navigation) where the focus is just locating objects or landmarks on them in image volumes and not delineating whole solid organs, a separate group of methods has been emerging (Criminisi et al., 2013; Donner et al., 2013). For all such approaches, it becomes essential to understand what normal anatomy is in a quantitative manner. Studies based on external and anthropometric measurements for the whole body as well as for specific body regions have been conducted (Robinette et al., 2002; Ressler, 1977; Wang et al., 2000; Nagamine and Suzuki, 1964; De Onis and Habicht, 1964). The anthropometry technique has been used to describe a broad set of measures: width, length, circumference, skin fold thickness, and distance among several landmarks.

* Corresponding author at: Medical Image Processing Group, Department of Radiology, University of Pennsylvania, 3710 Hamilton Walk, Goddard Building, 6th Floor, Rm 602, Philadelphia, PA 19104-6021, United States. Fax: +1 215 573 1811.
E-mail address: jay@mail.med.upenn.edu (J.K. Udupa).

http://dx.doi.org/10.1016/j.compmedimag.2016.03.005
0895-6111/© 2016 Elsevier Ltd. All rights reserved.

In the thoracic region, external measurements of circumference, anterior-posterior depth, and sternal size have been described in a systematic manner (Ressler, 1977). Yet, at present, assessment of normal internal thoracic anatomy in a comprehensive, quantitative, and three-dimensional manner is lacking.

Quantification of anatomy is required at different levels for AAR and quantitative radiology. On the one hand, for AAR, quantification at a more global level, such as through assessment of the overall morphology of individual objects and the inter-relationship among objects is needed. Such quantitative descriptions of a body region can greatly simplify and facilitate the task of automatically identifying and delineating all major objects in the body region by constructing population anatomic models of the objects and their geographic layout (Udupa et al., 2014). For example, Udupa et al. (2014) demonstrated how some of the quantitative anatomic properties, such as distance and size relationships among objects and their variation over a population, can be explicitly encoded in an anatomic hierarchical arrangement of all objects in a body region to handle any type of relationship (even non-linear) that may exist naturally among objects. Similarly, for every object, who its neighbors are and what their image intensity characteristics are constitute anatomic knowledge, which can also be encoded into the hierarchical object model assembly (Udupa et al., 2014). The hierarchical models can then be used to perform AAR. Such models can potentially be assessed to characterize age-related changes as proposed by Well et al. (2007). In the case of dynamic objects, the same type of quantitative entities as a function of time will also be useful. On the other hand, for quantitative radiology, the quantification is needed at a more detailed and local level. For example, individual object properties such as their volume, surface area, and shape characteristics (like boundary smoothness and roughness) have been used in describing disease processes rather than overall geography of objects and their relationships. As one example, we have recently shown (Tong et al., 2015) that, in obstructive sleep apnea syndrome (OSA), the bilateral fat pads (as 3D objects) are situated closer to oropharynx in OSA than in normal subjects. Conventionally, only the size of certain objects, mainly the adenoid and tonsils, have been the focus of study for understanding OSA and its treatment effects. Yet, over 50% of subjects treated with adeno-tonsillectomy continue to suffer from OSA. In this example, object relationship information has generated new knowledge on the potential causes of OSA. Perhaps a new way of treatment ought to be repositioning fat pad rather than removing tonsils and/or adenoid.

In the literature, quantification for describing normality is mainly confined to individual objects; quantification of object assemblies has not been studied. Some examples from the literature are as follows. The anatomic variants of vessel branching have been investigated, since such information may be useful for surgical purposes. For different structures, such as the portal vein, hepatic artery, and coronary arteries (Ibukuro et al., 2013; Mariolis-Sapsakos et al., 2012; Dal-Bianco and Levine, 2013; Młynarski et al., 2013; Vucurevic et al., 2013), the different branching patterns have been systematically described. Natsis et al. (2013) studied the morphometry of the foramen magnum and occipital condyles. Measurements such as diameter, length, and width were taken over dry skulls with a digital sliding caliper for a population study. There are other similar studies of the upper cervical spine for quantitatively describing the individual vertebrae (Radcliff et al., 2010; Simsek et al., 2013). In the thoracic region, the airway structure has been quantified by cross-sectional measures such as lumen area and wall thickness (Leader et al., 2008, 2006). An investigation by Sandoz et al. (2013) measured ribcage midline length, lateral and anteroposterior width, surface area, sternum volume, and cartilage to rib ratio. In all these examples, the focus was a single object or a part of an object and not an entire object assembly or body region or describing the geographic layout of an object assembly.

A more general and global approach to quantitatively describe the anatomy of a body region suits the spirit of quantitative radiology better for the purposes of AAR. Keeping the goal of AAR in mind, our aim in the current paper is to study normal anatomy quantitatively for individual and whole object assemblies in the thoracic body region. The methodology consists of collecting radiologically normal images from existing patient image databases, delineating all major objects in the body region in these images and creating object 3D surface models, analyzing the gross morphology of objects individually, and analyzing the inter-object relationships.

This paper presents new data on certain anatomic properties of and relationships among major objects of the thorax. The main motivation for excavating and understanding these data is automated localization and delineation of these objects in the entire thoracic body region. To the best of our knowledge such data do not exist in the literature at present. We have already demonstrated their use not just in the thoracic body region but also in other body regions and in fact body-wide (Udupa et al., 2014; Wang et al., 2016). Particularly, inter object relationships have been found to be highly non-linear and the incorporation of this information in an object hierarchy to localize objects in images automatically have been demonstrated to be a very effective approach (Udupa et al., 2014; Wang et al., 2016). Techniques based on registration which rely on smooth deformations cannot handle such non-linear relationships adequately. These findings have significant repercussions in many body-wide applications such as automatic contouring of objects for radiation therapy planning, body-wide disease quantification from PET/CT images, etc.

2. Materials & methods

2.1. Image Data

This retrospective study was conducted following approval from the Institutional Review Board at the Hospital of the University of Pennsylvania along with a Health Insurance Portability and Accountability Act (HIPAA) waiver. The image data utilized in this study were obtained from the radiology picture archiving and communication system. Forty-one 50–60 year old male subjects who had undergone thoracic contrast-enhanced computed tomography (CT) and whose CT images were considered to be radiologically normal by a board-certified radiologist were selected for the study. The routine chest CT examinations had been performed on 16 or 64 multidetector row CT scanners (Siemens Medical Solutions, Malvern, PA) during a full inspiratory breath hold and during the venous phase of enhancement. Images were acquired 50 s after intravenous administration of 100 ml of Isovue 370 iodinated contrast material (Bracco Diagnostic Inc., Princeton, NJ) at 2 ml/s with a slice collimation of 16×0.75 mm or 64×0.6 mm, respectively, a kVp of 120, an average effective tube current-time product of 200 mAs, with tube current modulation on, and a gantry rotation time of 0.5 s. Axial images were reconstructed at a nominal slice thickness of 5 mm with an interval of 5 mm, a 512×512 matrix, and a B30f reconstruction kernel. Each exam consisted of an average of 60 axial slices covering the entire thorax, with a pixel size of 0.77 mm $\times$ 0.77 mm.

2.2. Methods

The thoracic body region was defined consistently in terms of a starting and ending anatomic axial slice location for every subject—from 15 mm above the apex of the lungs to 5 mm below the base of the lungs. All collected image data were clipped to

Table 1
Objects studied in the thoracic region with their abbreviations and definitions.

Object	Abbreviation	Definition of object
Thoracic body region	ts	The outer boundary of the thoracic skin (arms excluded). The interior region constitutes the entire thoracic body region
Thoracic skeleton	sk	All skeletal structures contained in the thoracic body region
Respiratory system	rs = {rl, ll, tb}	Grouping of rl, ll, and tb
Right lung	rl	The outer boundary of the aerated right lung. Along the mediastinal pleural surface, the boundary was placed to exclude the large right hilar structures (distal right mainstem bronchus, bronchus intermedius, distal right main pulmonary artery, right interlobar pulmonary artery, perihilar portion of right superior pulmonary vein) while including other smaller right bronchial branches, right pulmonary arterial branches, right pulmonary venous branches, and aerated right lung as part of this object
Left lung	ll	The outer boundary of the aerated left lung. Along the mediastinal pleural surface, the boundary was placed to exclude the large left hilar structures (distal left mainstem bronchus, distal left main pulmonary artery, left interlobar pulmonary artery, perihilar portion of left superior pulmonary vein) while including other smaller left bronchial branches, left pulmonary arterial branches, left pulmonary venous branches, and aerated left lung as part of this object
Trachea and bronchi	tb	The outer boundary of the trachea and bronchi from the superior thoracic trachea to the distal intermediate bronchus on the right and the distal left main bronchus on the left
Internal mediastinum	im = {pc, es, as, vs}	Grouping of pc, es, as, and vs.
Pericardial region	pc	Region within the boundary of pericardial sac. The superior aspect is where the main pulmonary artery branches
Esophagus	es	The outer boundary of the esophagus from the superior slice through the thorax to the gastric cardia
Arterial system	as	The outer boundary of the ascending aorta, aortic arch, descending thoracic aorta, pulmonary arteries, innominate artery, proximal left common carotid artery, and proximal left subclavian artery. The superior aspect is where the innominate artery branches
Venous system	vs	The outer boundary of the superior vena cava, right and left brachiocephalic veins, and azygos vein

conform to this definition. Arms were excluded from the selected region. Similarly, each object within the thorax that was included in our study was defined consistently to indicate what aspects of the object are considered for inclusion in its spatial extent and its components. The 11 objects included in our study and their definitions are listed in Table 1. For all objects, the 3D region inside the indicated boundary is considered to be the object region.

Since our goal was to arrive at a quantitative description of the above thoracic-object assembly, we considered it important to delineate the objects as accurately as possible. Therefore, each of the 11 objects was carefully delineated in all 41 subject image sets by using a combination of image segmentation tools under close human supervision. The segmentation tools utilized included Live Wire (Falcão et al., 1998), Iterative Live Wire (Souza et al., 2006), thresholding, and manual outlining. In Live Wire, the user initially selects a point on the boundary of interest. The algorithm displays in real time the best of all possible paths from the initial point to the current position of the cursor as the user moves the mouse. If the cursor is placed close to the boundary the best path snaps on to the boundary. The cursor position is then deposited and the process continues. In Iterative Live Wire, the user traces the boundary on one slice and subsequently the next or the previous slice. The algorithm then automatically traces the boundary based on user action in the previous slice. If the delineation is acceptable, the user proceeds to subsequent slices in this manner. If the traced boundary is unacceptable, a fresh Live Wire tracing is done. We arrived at a procedure which combines the Live Wire strategies with manual tracing and thresholding etc. and the order in which objects are segmented so that the process is as efficient and accurate as possible. For example, once the skin outer boundary and the lungs are segmented by Iterative Live Wire, trachea and bronchi can be segmented more or less automatically by thresholding.

All results were checked for accuracy (by the two senior investigators in the team—DAT, a radiologist, and JKU, an imaging scientist, with 16 and 35 years of experience, respectively) via 3D surface renditions of each object separately and in different combinations with other objects for each subject. The 3D renditions provided a quick check for object consistency and for any errors in the form of any significant discontinuities from slice to slice. When errors were found in this manner, they were verified via slice displays of the delineations overlaid on the CT slices and then subsequently corrected. The most common errors that were found were slices with missing segmentations, which would appear as a dark slit through the object in 3D renditions, and discontinuities in boundary from slice to slice, which would appear as sudden protrusions or dents. Since these were both identified in 3D renditions and corrected, we believe that segmentation errors influenced our measurements minimally, if any.

The proposed quantitative description of thoracic anatomy was arrived at by employing two groups of measurements—the first describing the size, shape, and morphology of each object on its own, and the second describing the inter-relationship among objects. The individual measurements in each of these groups are described below in separate sections.

2.3. Object-specific measurements

For each object, its linear size estimates, surface area, sphericity, and CT attenuation properties were estimated.

2.3.1. Size (S_v and S_λ)

The idea behind a linear size estimate for an object is to express a measure of the "largeness" of the object within its population by a single number. This measure is useful in AAR for scaling objects (up or down) so that the same object from different subjects will have roughly the same "size" after scaling. We studied two measures, denoted S_v and S_λ, as described below.

$$S_v = \sqrt[3]{V}, \tag{1}$$

$$S_\lambda = \sqrt{\lambda_1 + \lambda_2 + \lambda_3}, \tag{2}$$

where V is the volume of the object in mm^3 and λ_1, λ_2, and λ_3 are the eigenvalues obtained by principal component analysis of the entire 3D object region. Roughly speaking, the eigenvalues indicate the variance (dispersion) of the object points in the three directions represented by the corresponding eigenvectors. The largest eigenvector, for example, indicates the direction of elongation of the object. S_v expresses the length of the side of a cube whose volume is equivalent to the object volume. S_λ roughly corresponds to

the length of the diagonal of a box that just encloses an ellipsoid approximating the object. Volume V was computed from the surface of the object which was approximated by a triangular mesh (Nystrom et al., 2011).

2.3.2. Surface area (SA)

The surface area of each object was computed by first representing the object surface as a triangle mesh from the given 3D binary image of the object, and then computing the total area (Nystrom et al., 2011).

2.3.3. Sphericity (Sp)

This is a unit-less measure which expresses object shape complexity as compared to a sphere. It expresses how an object deviates from being spherical. The formula given below, which is dependent on volume V and surface area SA of the object, is derived in such a manner that for a sphere this number is the highest and equals 1. For all other shapes, it will have lower values. For example, for a cube, Sp = 0.806, and for a cylinder of equal height and radius, Sp = 0.825. As the object shape increases in complexity, the object's SA increases relative to its volume, and so Sp becomes smaller. Note that different shapes can have the same sphericity value.

$$\mathrm{Sp} = \frac{\sqrt[3]{36\pi V^2}}{\mathrm{SA}}. \tag{3}$$

2.3.4. Image intensity-based measures (HU_M, HU_{Md}, HU_P, HU_{Q1}, HU_{Q3})

CT image intensity values characterize the X-ray attenuation properties, expressed in Hounsfield Units (HU), of the tissues composing the object. We computed HU statistics including mean (HU_M), median (HU_{Md}), mode (HU_P), and the first and third quartiles (HU_{Q1} and HU_{Q3}) within the entire 3D region occupied by the object in its native image for each object considered in our study.

Mean HU properties for different types of tissues – muscle, fat, lung tissue, cortical bone, etc. – are generally known and available in radiology textbooks, but are not available for many of the objects we have considered in this paper. In addition, information regarding the variability of HU measures of various tissues (whether based on standard deviation or quartile measures) is not included in radiology textbooks. Whether or not the HU properties overlap from object to object and by how much are by themselves useful pieces of information for anatomy recognition. In addition, knowledge of the normal HU properties of the thoracic objects of interest is important to help to distinguish them from abnormal conditions or lesions that may affect the thoracic objects and alter their HU properties.

2.3.5. Normalization

Among the measurements described above, S_v, S_λ, and SA are absolute measures. When studying these variables, it is important to adjust them to account for variation in the size of individual subjects. It is expected that larger individuals will have overall larger objects. To make this adjustment, we normalized these measurements by dividing them by the length of the diagonal of a box that encloses the thoracic skeleton, the idea being that the skeleton encloses the thoracic region, constraining other objects, and is a good indicator of the overall size of a subject. If L denotes this normalizing length for a subject, then the normalized size measures were expressed as S_v/L, S_λ/L, and SA/L^2.

2.4. Inter-object relationships

Object relationships were studied in three ways—in terms of the distances between every pair of objects, the correlation among objects in their object-specific measures, and the correlation among objects between distances and between distance and some of the size measures.

2.4.1. Distances between objects (d(A, B))

The geometric center of each object was taken to be its reference point, and the distance $d(A, B)$ between two objects A and B was defined as the Euclidean distance between their geometric centers. Note that the geometric center may not always be inside the object. For instance, for pericardial region, this point is inside the object. However, the thoracic skeleton (with the rib cage and the vertebral column) has a complex shape with an "empty" space in the center, and the geometric center is outside the solid object and in this central region. The manner in which the centers are distributed has interesting overall anatomic information about how objects are geographically laid out in the thorax.

2.4.2. Correlation among objects based on object-specific measures

To study object relationships in terms of their object-specific measures, we calculated the Pearson coefficient of correlation between every pair of objects for each of the measures S_v/L, S_λ/L, SA/L^2, and Sp. For each measure, the correlations were computed as (symmetric) correlation matrices. For better visual depiction of the correlations, we used a color graphical method called *heat map* (Souza et al., 2006). In heat map visualization, the columns and rows of the matrix are organized by similarity in a way that similar behaving rows and columns are clustered automatically. The advantage of the heat map over numerical correlation matrices is better global, quick, and intuitive visualization of the information in an organized manner. The magnitude of the correlations is expressed on a heated color scale from dark blue to dark red, where blue, red, and white correspond to negative, positive, and no correlation, respectively.

2.4.3. Correlation among objects in their distances

For all possible combinations of 4 objects A, B, C, and D, we studied the correlation between distances $d(A, B)/L$ and $d(C, D)/L$ over the subject population. Note that, A, B, C, and D are distinct objects except that B and C may or may not denote the same object. For example, with A = sk, B = pc, C = pc, D = as, we can study the correlation between distance from the pericardial region to the thoracic skeleton and distance from pericardial region to the arterial system. With A = sk, B = pc, C = es, and D = as, we can study the correlation between the distance from pericardial region to the thoracic skeleton and distance from the arterial system to esophagus. With 11 objects in the thoracic region, there are a total of 55 combinations of distances between two distinct objects, and hence a total of 1485 coefficients of correlation. Again we employ the heat maps to depict these relationships in distances.

2.4.4. Correlation among objects between distance and object-specific measures

For all possible combinations of 3 objects A, B, and C, we analyzed the correlation between $d(A, B)/L$ and the size measures S_v/L and S_λ/L of C. Note here that objects B and C may or may not be the same. For example, with A = sk, B = pc, and C = pc, we can study the correlation between distance from the thoracic skeleton to the pericardial region and any of the size measures of the pericardial region. With A = sk, B = pc, and C = es, we can study the correlation between distance from the thoracic skeleton to the pericardial region and any of the size measures of the esophagus. There are 605 distinct coefficients of correlation in this manner for each size measure.

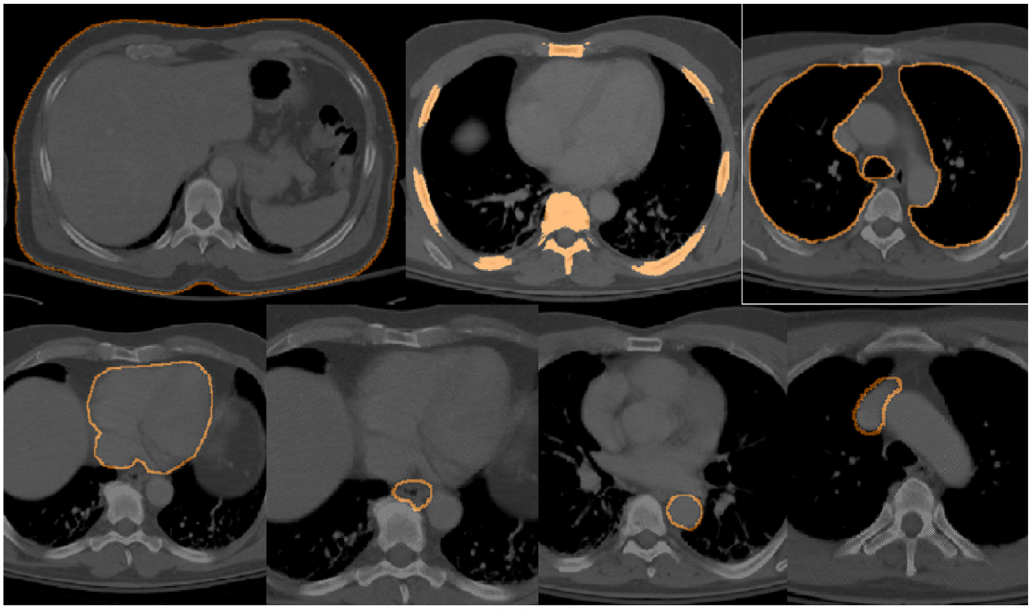

(a)

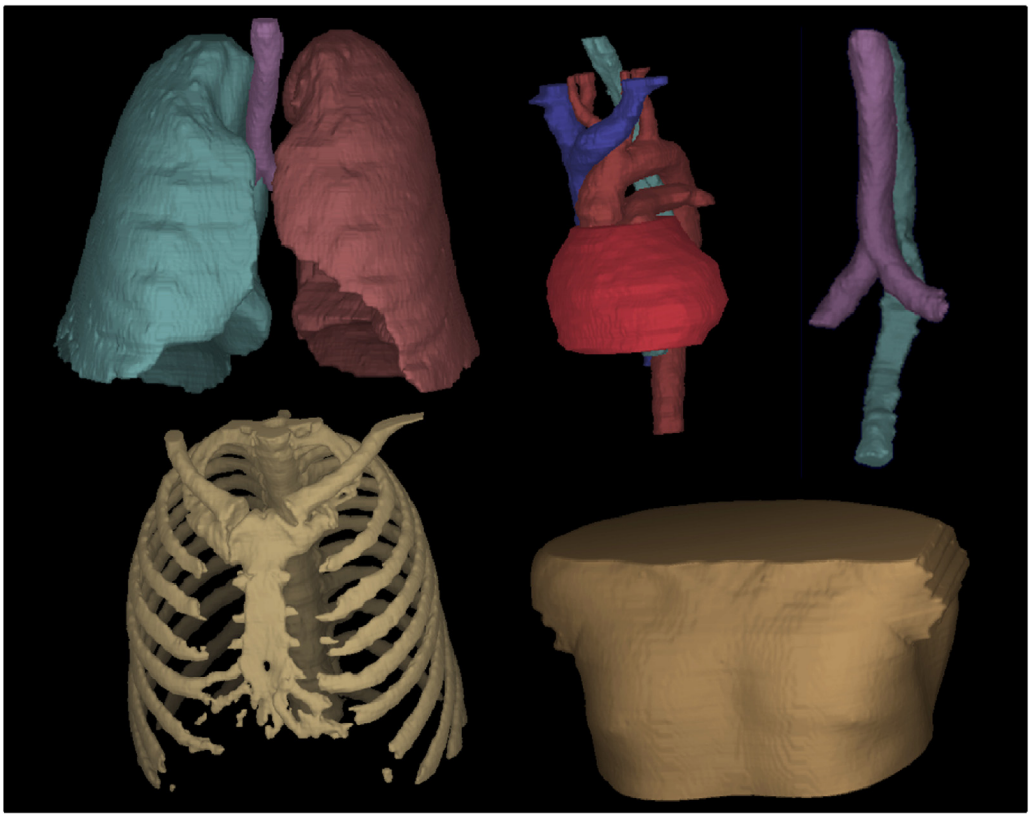

(b)

Fig. 1. (a) Object segmentations for one subject. Left to right, top to bottom: boundaries of skin, skeleton, right lung & left lung, trachea & bronchi, pericardial region, esophagus, arterial system, and venous system. (b) 3D visualization of some of the objects for one subject. Top left: right lung, trachea & bronchi, and left lung. Top center: pericardial region, arterial system, venous system, and esophagus. Top right: trachea & bronchi and esophagus. Bottom left: thoracic skeleton. Bottom right: thoracic skin.

3. Results

To illustrate the nature and spatial arrangement of the different objects considered in this study, they are depicted in Fig. 1 via their segmentations and surface renditions for one subject.

3.1. Object-specific measures

The mean and standard deviation of the four measures S_v/L, S_λ/L, SA/L^2, and Sp estimated over the subject population are summarized in Table 2. The statistics of the HU values for the different objects over the studied population are portrayed in Table 3.

Table 2
Mean, standard deviation, and coefficient of variation of Sv/L, S_λ/L, SA/L^2, and Sp for the 11 objects in the thoracic region ($N = 41$). Object abbreviations: ts—thoracic skin, sk—thoracic skeleton, rs—respiratory system, rl—right lung, ll—left lung, tb—trachea & bronchi, im—internal mediastinum, pc—pericardial region, es—esophagus, as—arterial system, vs—venous system.

Object	S_v/L		S_λ/L		SA/L^2		Sp	
	Mean (sd)	CV%	Mean (sd)	CV%	Mean (sd)	CV%	Mean (sd)	CV%
ts	0.551 (0.030)	6.4	0.282 (0.015)	6.0	1.901 (0.205)	10.8	0.776 (0.022)	2.8
sk	0.216 (0.013)	5.5	0.243 (0.013)	5.8	1.891 (0.235)	12.4	0.119 (0.006)	4.7
rs	0.337 (0.031)	10.3	0.21 (0.014)	7.8	1.323 (0.194)	14.7	0.401 (0.021)	5.2
rp	0.273 (0.024)	9.9	0.154 (0.013)	9.4	0.675 (0.097)	14.4	0.536 (0.026)	4.9
lp	0.260 (0.026)	11.2	0.154 (0.013)	10.0	0.639 (0.098)	15.3	0.513 (0.033)	6.4
tb	0.072 (0.007)	8.7	0.088 (0.08)	8.0	0.055 (0.009)	16.9	0.454 (0.024)	5.4
im	0.206 (0.013)	6.1	0.126 (0.008)	6.3	0.529 (0.062)	11.7	0.387 (0.016)	4.1
pc	0.183 (0.012)	6.0	0.093 (0.006)	6.1	0.225 (0.028)	12.4	0.726 (0.023)	3.1
es	0.071 (0.006)	7.8	0.144 (0.015)	11.8	0.068 (0.011)	16.2	0.357 (0.021)	5.9
as	0.131 (0.014)	11.2	0.124 (0.014)	12.3	0.253 (0.038)	15.0	0.340 (0.012)	3.5
vs	0.075 (0.007)	7.4	0.107 (0.012)	11.2	0.082 (0.014)	16.7	0.329 (0.026)	7.8

Table 3
Hounsfield Unit statistics for the different objects: mean (HU_M), standard deviation (HU_{SD}), median (HU_{Md}), mode (HU_P), and quartiles (HU_{Q1} and HU_{Q3}) ($N = 41$). Object abbreviations: ts—thoracic skin, sk—thoracic skeleton, rs—respiratory system, rl—right lung, ll—left lung, tb—trachea & bronchi, im—internal mediastinum, pc—pericardial region, es—esophagus, as—arterial system, vs—venous system.

	HU_M	HU_{SD}	HU_{Md}	HU_P	HU_{Q1}	HU_{Q3}
ts	−137.3	52.6	12	73	−150	83
sk	306.9	49.9	269	217	181	396
rs	−761.0	64.8	−816	−850	−858	−739
rl	−760.7	59.2	−815	−850	−857	−741
ll	−759.5	75.0	−815	−857	−858	−736
tb	−846.7	56.3	−934	−1000	−962	−833
im	147.0	39.5	143	171	87	194
pc	136.1	37.4	134	103	83	186
es	−0.1	50.9	49	57	8	74
as	182.4	40.5	180	177	144	217
vs	302.2	146.1	153	72	68	392

3.2. Inter-object relationships

Correlations among objects in object-specific measures S_v/L, S_λ/L, SA/L^2, and Sp are depicted in Fig. 2 as heat maps. Correlations between distance measures $d(A, B)/L$ and $d(C, D)/L$ are displayed in Fig. 3, and between distance $d(A, B)/L$ and the size measures S_v/L and S_λ/L in Fig. 4, via heat maps.

4. Discussion

4.1. Object-specific measures

From Table 2, we observe that the normalized size S_v/L ranges from 0.071 (for esophagus) to 0.551 (for the entire thoracic body region) and S_λ/L varies from 0.093 (for the pericardial region) to 0.282 (for the entire thoracic body region). That is, as per both measures, thoracic skin is the largest object, but the smallest object depends on our viewpoint—esophagus for the first measure and pericardial region for the second (since pericardial region has the smallest elongation). The coefficient of variation over the studied population is the smallest for thoracic skeleton for both measures, as may be expected, since it was used as the reference for normalizing the measures. Interestingly, pericardial region has a low coefficient of variation for S_v/L, suggesting that normalized heart size does not vary much from subject to subject. The difference between the two size measure is expressed well by the three tubular structure trachea & bronchi, venous system, and esophagus, which have approximately the same S_v/L values (0.07), although their S_λ/L values range from 0.088 (trachea & bronchi) to 0.144 (esophagus), suggesting that although the three objects have similar volumes, their shapes are different. Similarly, per S_v/L, the right lung is typically larger than the left lung; however, S_λ/L is the same for both lungs, meaning that although the lungs have different volumes, their elongations are similar.

The sphericity (Sp) values listed in Table 2 contain information about the gross shape of the objects in terms of their deviation from a sphere. Blob-like objects (skin and pericardial region) have Sp values close to 1, whereas sparse and less space-filling objects such as the thoracic skeleton (Sp = 0.119) and the arterial and venous systems (Sp = 0.349 and 0.329, respectively) have much lower values. The normalized surface area (SA/L^2) values range from 0.055 (trachea & bronchi) to 1.901 (skin). The thoracic skeleton has an average normalized surface area of 1.891, which is close to that of the thoracic body region, in spite of it being a smaller, less space filling object overall.

From Table 3, we observe that the lungs and the trachea & bronchi have the lowest attenuation values, close to −1000 HU, whereas soft tissue structures (arterial system, esophagus, pericardial region, internal mediastinum) occupy a middle range of attenuation values as expected. Both the skeleton and venous system exhibit a large inter-quartile range (HU_{Q3}–HU_{Q1}) of attenuation due to variable amounts of contrast material in the venous system and due to the large variation in bone composition (from cortical bone to medullary trabecular bone to bone marrow) in the skeleton. Since by definition the skin object contains the entire thoracic body region (see Table 1), it also exhibits a large inter-quartile range, although at a much lower median value than the skeleton and venous system. There are other investigations which studied HU properties of thoracic objects. For example, Corson et al. (2011) compared HU distributions of select tissues, mesothelioma, muscle, and liver across three different scanners and reconstruction filter/kernels. HU distribution of fat was found to have the least overlap with other tissues. Separating mesothelioma, muscle, and liver from one another however was difficult based on HU value thresholding alone. As mentioned earlier, our motivation for studying HU properties in this work goes beyond characterization of individual tissues to building population models of the entire anatomy in a body region, using HU properties to optimally recognize objects, and to optimally delineate objects based on HU properties of the objects in a neighborhood (Udupa et al., 2014). We however also note that since this study was carried out with a contrast medium, some of the above observations will change in non-contrast studies. Particularly, the HU statistics within the arterial system, venous system, and pericardial region and composite objects that contain these structures such as the skin object and internal mediastinum may change.

Since all object-specific measures are normalized either explicitly (S_v/L, S_λ/L, SA/L^2) or implicitly (Sp and all HU measures), they

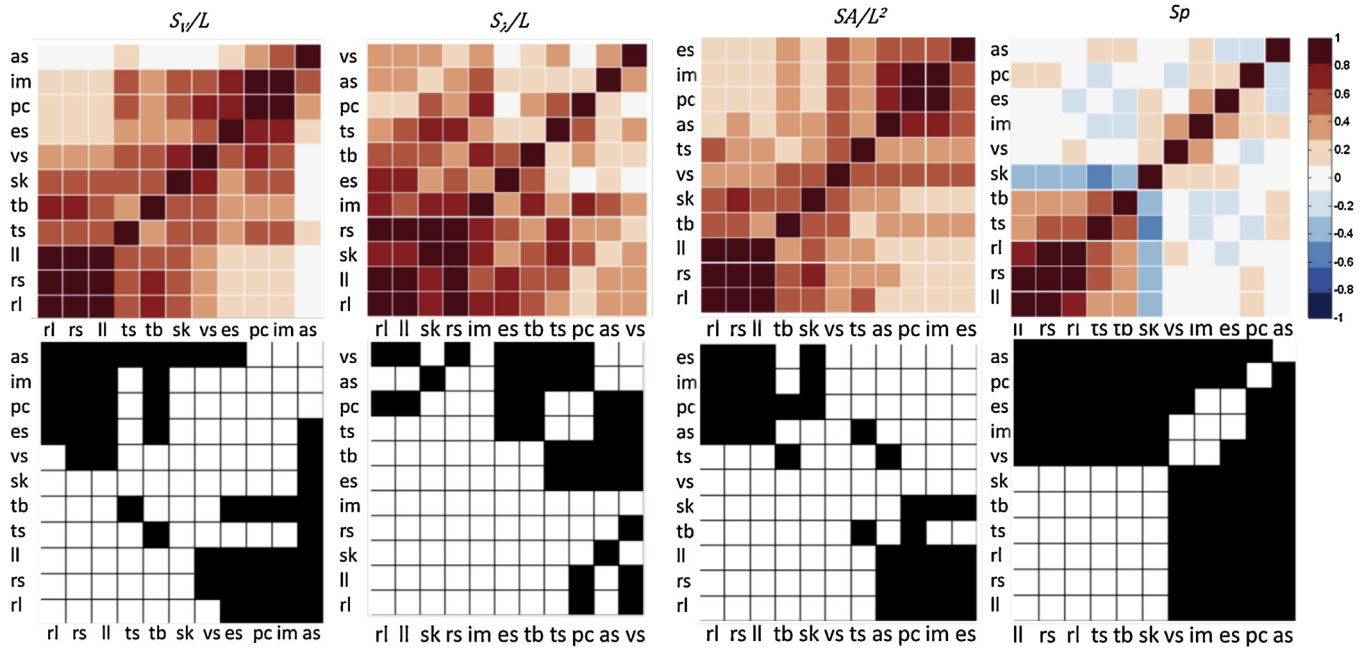

Fig. 2. Coefficients of correlation among objects depicted via heat maps for object-specific measures S_v/L, S_λ/L, SA/L^2, and Sp. The corresponding p-value maps, where $p < 0.05$ is displayed in white, are also shown below the heat maps. Object abbreviations: ts—thoracic skin, sk—thoracic skeleton, rs—respiratory system, rl—right lung, ll—left lung, tb—trachea & bronchi, im—internal mediastinum, pc—pericardial region, es—esophagus, as—arterial system, vs—venous system.

Table 4
List of key objects and their involved distances that showed strong correlations. Object abbreviations are as follows: ts—thoracic skin, sk—thoracic skeleton, rs—respiratory system, rl—right lung, ll—left lung, tb—trachea & bronchi, im—internal mediastinum, pc—pericardial region, es—esophagus, as—arterial system, vs—venous system.

Key objects	Involved distances
tb	d(pc, tb), d(pc, tb), d(tb, ts), d(sk,tb), d(tb, rl), d(tb, ll), d(rs, tb)
vs	d(vs, pc), d(vs, im), d(rs, vs), d(vs, ts), d(vs, rl), d(vs, ll)
as	d(rs, as), d(as,sk), d(as,tb), d(es, as), d(vs, as), d(im, as), d(pc, as), d(as,rl), d(as,ll)
im	d(im,rs), d(im,ts), d(im,ll)
es	d(im, es), d(pc,es), d(rs,es), d(es, sk), d(es, ts)

can be readily used in a quantitative radiology system to compare measures derived from patients against normative values as obtained in the present study. We took the skeletal structure as the basis for normalizing all measures, which we believe is a reasonable attitude. It is hard to ascertain how good this normalization scheme is, for example, in case of excessive visceral or subcutaneous adiposity. This leads us to a fundamental question of what normalization means when everything is variable. What is important, we believe, is that normalization is done in the same consistent manner and that the measurements generated are found useful. Determining the relative effectiveness of different normalization schemes in this sense obviously requires further research.

4.2. Inter-object relationships

From Fig. 2, the most correlated objects by the size measures $S_v/L$and S_λ/L (with coefficient of correlation > 0.82) are bilateral objects in the thorax such as right lung and left lung. A similar observation also applies to objects which are supersets, such as respiratory system rs = {rl, ll, tb} and internal mediastinum im = {as, vs, es, pc}. In the latter case, there is high correlation between the superset object and its members, such as between respiratory system and left lung, internal mediastinum and pericardial region, etc. Both observations make sense since we expect the compared objects to vary together in size from subject to subject. In general, most pairs of objects have positive correlation values, although the relationships are different for each pair. The correlations between the pericardial region and the respiratory objects are insignificant, which suggests that normalized heart and lung sizes do not vary together linearly from subject to subject as the subject size changes. It is worth noting that the pericardial region size, as per Table 2, has low coefficient of variation. Such information is extremely useful in developing effective models for performing AAR by designing hierarchical arrangement of objects where least varying objects are located first with respect to whom other objects can be identified in the hierarchy (Matsumoto and Udupa, 2013). Another salient non-statistically significant relationship is that of the vascular systems (as and vs) to other objects in the thorax. Note also that these objects are among those with the highest coefficients of variation. The measures of SA/L^2 also reveal similar trends as S_v/L of higher levels of correlation for bilateral objects and superset objects. The measures of Sp presented a positive correlation among the respiratory objects and the skin object, meaning that shape complexities of these objects as measured by Sp vary in the same manner from subject to subject. Interestingly, Sp values exhibit a negative correlation between the thoracic skeleton and both the respiratory objects and the entire thoracic body region. This implies that as the skeleton becomes more complex in shape, the respiratory objects and skin lose their shape complexity and become rounder.

From Fig. 3 we observe that there are regions in the heat map with positive correlation values. These pockets are related to structures with interesting distance values. For instance, the first region in the lower left corner is related to distances with respect to trachea & bronchi taken as a central structure. In this region, the following distances have a strong positive correlation where trachea & bronchi as an object plays a central role: d(pc, tb), d(im,tb),

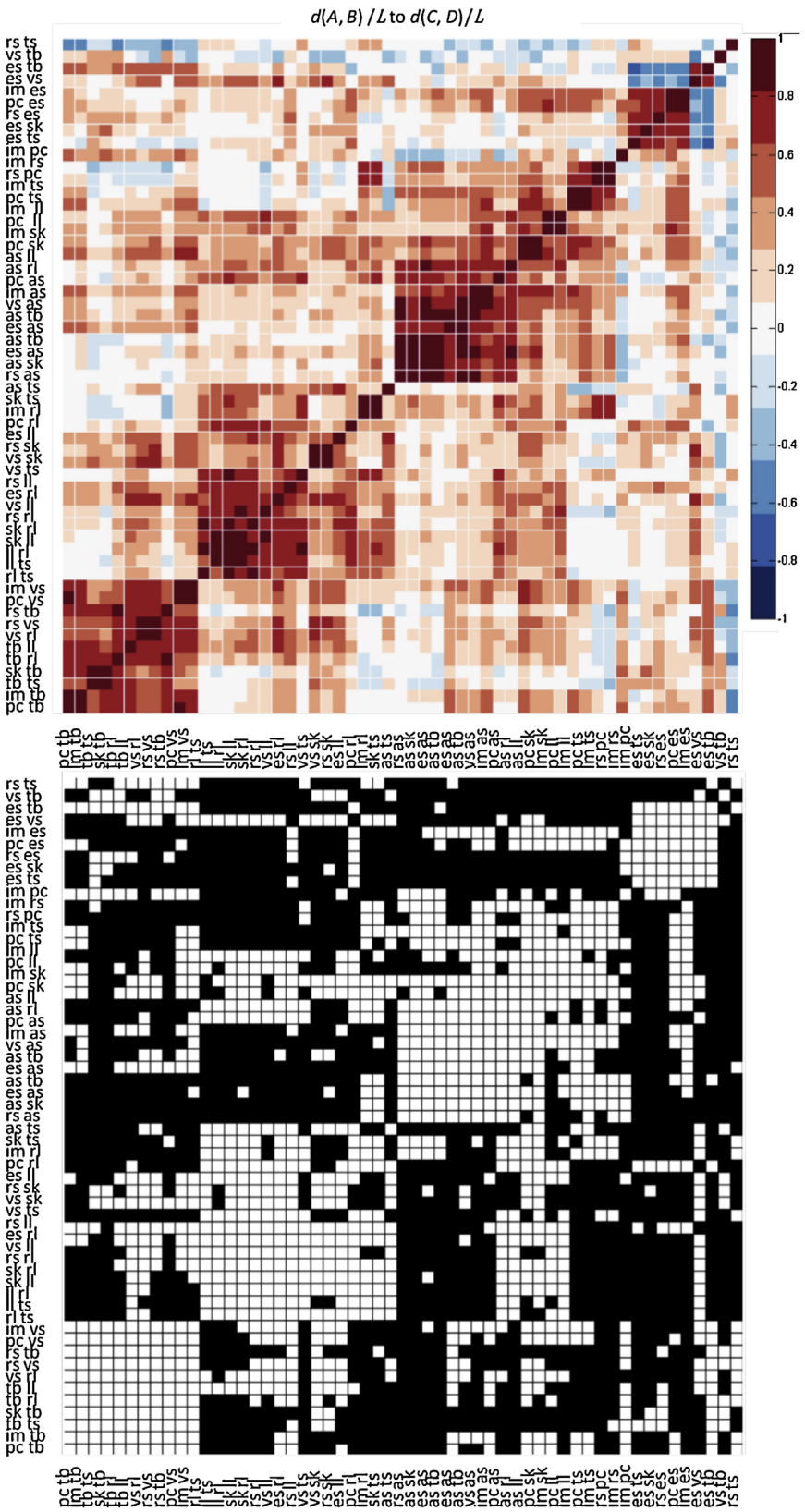

Fig. 3. Coefficient of correlation between $d(A, B)/L$ and $d(C, D)/L$ displayed as a heat map. The corresponding p-value map, where $p < 0.05$ is shown in white, is also displayed below the heat map. Object abbreviations: ts—thoracic skin, sk—thoracic skeleton, rs—respiratory system, rl—right lung, ll—left lung, tb—trachea & bronchi, im—internal mediastinum, pc—pericardial region, es—esophagus, as—arterial system, vs—venous system.

d(tb, ts), d(sk,tb), d(tb, rl), d(tb, ll), d(vs, rl), d(rs, vs), d(rs, tb), d(pc, vs), and d(im, vs). Likewise, the objects which are central to other regions are right lung and left lung, arterial system, and esophagus. We have listed in Table 4 the key central objects and the

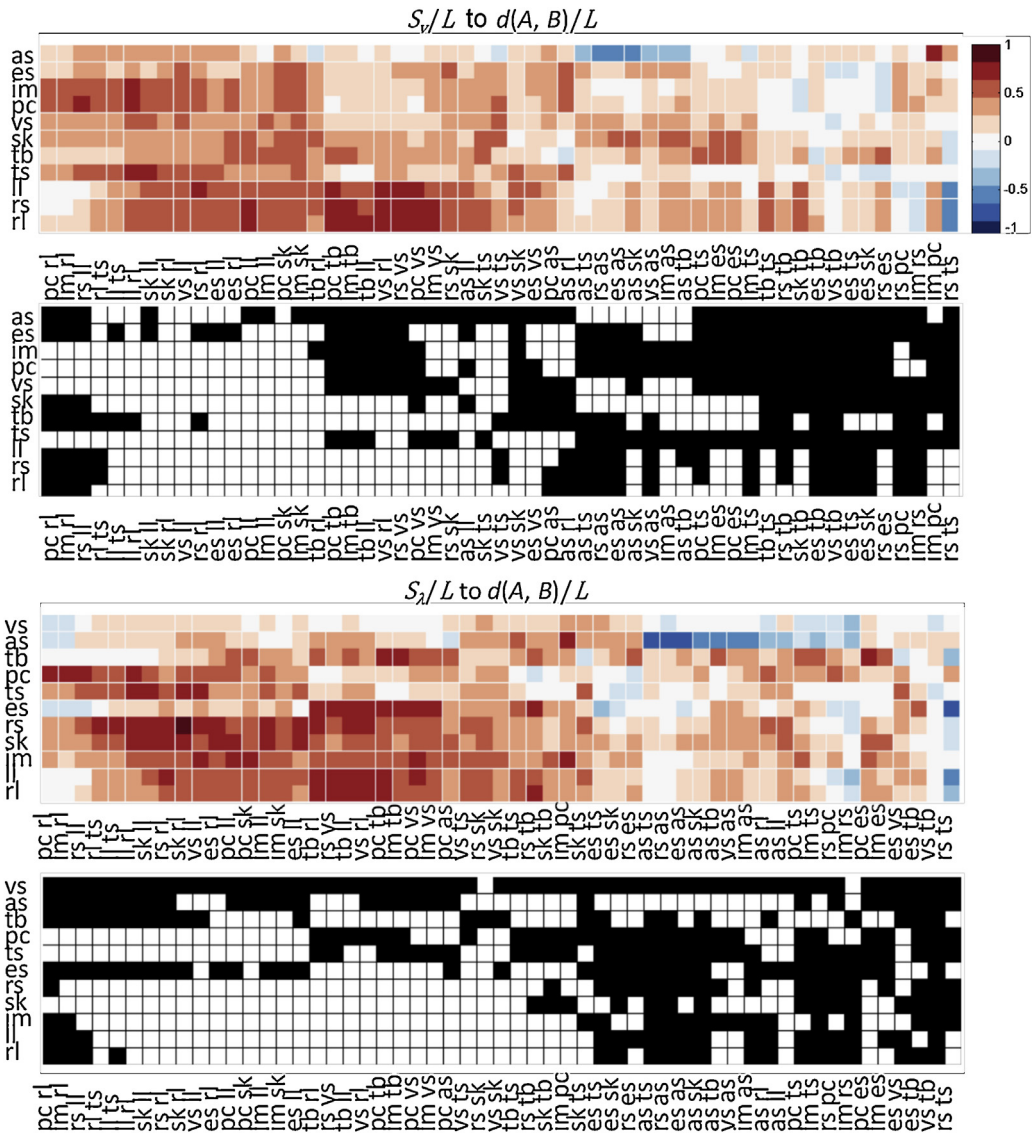

Fig. 4. Coefficient of correlation between $d(A, B)/L$ and S_v/L, and $d(A, B)/L$ and S_λ/L. The corresponding p-value maps, where $p < 0.05$ is shown in white, are also displayed below the heat maps. Object abbreviations: ts—thoracic skin, sk—thoracic skeleton, rs—respiratory system, rl—right lung, ll—left lung, tb—trachea & bronchi, im—internal mediastinum, pc—pericardial region, es—esophagus, as—arterial system, vs—venous system.

involved distances that showed strong correlation. Such objects that bind other objects in strong relationships can be useful in AAR to automatically locate other objects in given images; see below.

In Fig. 4, we observe that the S_v variations are positively correlated with the distances between the objects, but not very strongly, as most of the correlations are in the range of (0.09–0.64). There are a few negative correlations as well, such as the size of arterial system to the distance between this object and the respiratory system. The same is true for S_λ to distance correlations, but there are also stronger associations, such as of the size of respiratory system to d(sk, rl). In this case also, the negative correlations are related to the size of the arterial system and distances among skeleton, respiratory system, and esophagus.

The AAR methodology of Udupa et al. (2014) organizes all objects in a body region into a hierarchy as a tree structure for creating body-wide models and for using them for automatic recognition and delineation of objects (Udupa et al., 2014). In the AAR framework, the knowledge of object relationships (in terms of size and shape correlations, distance-to-size correlations, and distance-to-distance correlations) brings salient population anatomic knowledge to be encoded into the models. For example, in the hierarchy of objects, it makes sense to have an object A which has a strong relationship with another object B as an offspring of object B. Such knowledge helps in designing optimal arrangements of objects in a hierarchy for automatic object recognition and delineation with high accuracy. For some early results which utilized such information, see Falcão et al. (1998).

5. Concluding remarks

In this paper, we presented a methodology to investigate the quantitative aspects of normal thoracic anatomy on CT. We assessed normal values of attenuation, size, surface area, and shape of major objects (including object combinations) in the thoracic region, as well as of the relationships of sizes and distances among different objects. Within the quantitative radiology perspective, quantification provides objective knowledge about normal anatomy. More importantly, the analysis of correlation highlights what the prominent relationships are among normal objects. Bilateral objects in the thoracic region tend to have tight

size relationships. Some of the distances between thoracic objects are more consistent with other distances if taken from an object such as trachea and bronchi. All this information can be translated, for instance, to devise better population models for AAR, which was the underlying motivation for this study.

Our study has some limitations. First, the number of subjects ($N = 41$) we studied is relatively small, but served to provide preliminary data that may be useful to investigate larger subject populations in the future. While the number of data sets considered in this paper is rather small, we focused on a narrow age group and not the entire adult subject population. Also, we note that in many studies (actually most published papers on atlas- and model-based methods), the number of data sets used for building the model/atlas is about the same or even less than the number of data sets considered in this paper. Second, we focused on only one subject group (50–60 year old men) in this study, and therefore some or all of our observations may be specific only to this demographic group. However, the approach presented can be applied to other subject populations in order to assess the generalizability of the results. Third, for ease of data collection and considerations of cost, we used existing patient images that were considered to be normal based on thoracic CT imaging. It is possible that some of these subjects may have had clinical abnormalities that were not detectable on CT. These limitations need to be addressed in the future from the perspective of quantitative radiology. However, for AAR they do not matter, since effective population models can be built from such a sample size and utilized in object detection and delineation as already demonstrated (Udupa et al., 2014). We already have evidence that the quantitative knowledge of the kind described in this paper is very useful to develop generalizable AAR methods (Udupa et al., 2014). Other correlations that we have not analyzed such as among object-specific measures (between S_λ and HU variables, S_λ and Sp, Sp and HU variables, etc.) and among distances and other object-specific measures may also reveal useful information.

References

Baiker, M., Milles, J., Dijkstra, J., Henning, T.D., Weber, A.W., Que, I., Kaijzel, E.L., Lowik, C.W., Reiber, J.H., Lelieveldt, B.P., 2010. Atlas-based whole-body segmentation of mice from low-contrast Micro-CT data. Med. Image Anal. 14, 723–737.

Cabezas, M., Oliver, A., Llado, X., Freixenet, J., Cuadra, M.B., 2011. A review of atlas-based segmentation for magnetic resonance brain images. Comput. Methods Programs Biomed. 104, e158–177.

Chen, X., Bagci, U., 2011. 3D automatic anatomy segmentation based on iterative graph-cut-ASM. Med. Phys. 38, 4610–4622.

Chen, Q., Quan, F., Xu, J., Rubin, D.L., 2013. Snake model-based lymphoma segmentation for sequential CT images. Comput. Methods Programs Biomed. 111, 366–375.

Cootes, T.F., Taylor, C.J., Cooper, D.H., Graham, J., 1995. Active shape models-their training and application. Comput. Vis. Image Underst. 61 (1), 38–59.

Corson, N., Sensakovic, W.F., Straus, C., Starkey, A., Armato 3rd, S.G., 2011. Characterization of mesothelioma and tissues present in contrast-enhanced thoracic CT scans. Med. Phys. 38, 942–947.

Criminisi, A., Robertson, D., Konukoglu, E., Shotton, J., Pathak, S., White, S., Siddiqui, K., 2013. Regression forests for efficient anatomy detection and localization in computed tomography scans. Med. Image Anal. 17, 1293–1303.

Dal-Bianco, J.P., Levine, R.A., 2013. Anatomy of the mitral valve apparatus: role of 2D and 3D echocardiography. Cardiol. Clin. 31, 151–164.

De Onis, M., Habicht, J.P., 1964. Anthropometric reference data for international use: recommendations from a World Health Organization Expert Committee. Am. J. Clin. Nutr. 64 (4), 650–658.

Donner, Rene, Menze, Bjoern H., Bischof, Horst, Langs, Georg, 2013. Global localization of 3D anatomical structures by pre-filtered Hough forests and discrete optimization. Med. Image Anal. 17, 1304–1314.

Evans, A.C., Janke, A.L., Collins, D.L., Baillet, S., 2012. Brain templates and atlases. NeuroImage 62, 911–922.

Falcão, A.X., Udupa, J.K., Samarasekera, S., 1998. User-steered image segmentation paradigms: live wire and live lane. Graph. Models Image Process. 60 (4), 233–260.

Ibukuro, K., Takeguchi, T., Fukuda, H., 2013. Spatial relationship between the hepatic artery and portal vein based on the fusion image of CT angiography and CT arterial portography: the left hemiliver. AJR Am. J. Roentgenol. 200 (5), 1160–1166.

Jia, H., Yap, P.T., Shen, D., 2012. Iterative multi-atlas-based multi-image segmentation with tree-based registration. NeuroImage 59, 422–430.

Joshi, S., Davis, B., Jomier, M., Gerig, G., 2004. Unbiased diffeomorphic atlas construction for computational anatomy. NeuroImage 23 (Suppl. 1), S151–160.

Leader, J.K., Zheng, B., Scuirba, F.C., 2006. Airway morphometry in the lungs as depicted in chest CT examinations variability of measurements. Proceedings of SPIE 2006 Medical Imaging vol. 6143, 61432.

Leader, J.K., Zheng, B., Sciurba, F.C., 2008. The relation of airway size to lung function. Proceedings of SPIE 2008 Medical Imaging vol. 6916, 691623.

Młynarski, R., Młynarska, A., Sosnowski, M., 2013. Anatomical variants of left circumflex artery, coronary sinus and mitral valve can determine safety of percutaneous mitral annuloplasty. Cardiol. J. 20 (3), 235–240.

Mariolis-Sapsakos, T., Kalles, V., Papatheodorou, K., Goutas, N., Papapanagiotou, I., Flessas, I., Kaklamanos, I., Arvanitis, D.L., Konstantinou, E., Sgantzos, M.N., 2012. Anatomic variations of the right hepatic duct: results and surgical implications from a cadaveric study. Anat. Res. Int. 2012, 838179.

Matsumoto, M.M., Udupa, J.K., 2013. Optimal hierarchies for fuzzy object models. Proceedings of SPIE 2013 Medical Imaging vol. 8671, 86712.

Nagamine, S., Suzuki, S., 1964. Anthropometry and body composition of Japanese young men and women. Hum. Biol. 36, 8–15.

Natsis, K., Piagkou, M., Skotsimara, G., Piagkos, G., Skandalakis, P., 2013. A morphometric anatomical and comparative study of the foramen magnum region in a Greek population. Surg. Radiol. Anat. 35, 925–934.

Nystrom, I., Grevera, G.J., Hirsch, B.E., Udupa, J.K., 2011. Efficient computation of enclosed volume and surface area from the same triangulated surface representation. Comput. Med. Imaging Graph. 35, 460–471.

Okada, T., Yokota, K., Hori, M., Nakamoto, M., Nakamura, H., Sato, Y., 2008. Construction of hierarchical multi-organ statistical atlases and their application to multi-organ segmentation from CT images. Med. Image Comput. Comput. Assist. Interv. 11, 502–509.

Radcliff, K.E., Ben-Galim, P., Dreiangel, N., 2010. Comprehensive computed tomography assessment of the upper cervical anatomy: what is normal? Spine J. 10 (3), 219–229.

Ressler, S., 1977. AnthroKids—Anthropometric Data of Children. National Institute of Standards and Technology http://ovrt.nist.gov/projects/anthrokids.

Robinette, K.M., Blackwell, S., Daanen, H., Boehmer, M., Fleming, S., 2002. Civilian American and European Surface Anthropometry Resource (CAESAR), Final Report, vol. 1. Summary. DTIC Document.

Sandoz, B., Badina, A., Laporte, S., Lambot, K., Mitton, D., Skalli, W., 2013. Quantitative geometric analysis of rib, costal cartilage and sternum from childhood to teenagehood. Med. Biol. Eng. Comput. 51, 971–979.

Simsek, S., Uz, A., Er, U., Apaydin, N., 2013. Quantitative evaluation of the anatomical parameters for subaxial cervical spondylectomy: an anatomical study. J. Neurosurg. 18, 568–574.

Souza, A., Udupa, J.K., Grevera, G., 2006. Iterative live wire and live snake: new user-steered 3D image segmentation paradigms. Proceedings of SPIE 2006 Medical Imaging vol. 6144, 61443.

Tong, Y., Udupa, J.K., Torigian, D.A., Sin, S., Raanan, A., 2015. MR image analysis of upper airway architecture in children with OSAS. Proceedings of SPIE, Medical Imaging 2015 vol. 9417, 94172J1–94176.

Udupa, J.K., Odhner, D., Zhao, L., Tong, Y., Matsumoto, M.M., Ciesielski, K.C., Falcao, A.X., Vaideeswaran, P., Ciesielski, V., Saboury, B., Mohammadianrasanani, S., Sin, S., Arens, R., Torigian, D.A., 2014. Body-wide hierarchical fuzzy modeling, recognition, and delineation of anatomy in medical images. Med. Image Anal. 18, 752–771.

Vucurevic, G., Marinkovic, S., Puskas, L., Kovacevic, I., Tanaskovic, S., Radak, D., Ilic, A., 2013. Anatomy and radiology of the variations of aortic arch branches in 1,266 patients. Folia Morphol. 72, 113–122.

Wang, J., Thornton, J.C., Kolesnik, S., Pierson Jr., R.N., 2000. Anthropometry in body composition: an overview. Ann. N. Y. Acad. Sci. 904, 317–326.

Wang, H., Udupa, J.K., Odhner, W., Tong, Y., Zhao, L., Torigian, D.A., 2016. Automatic anatomy recognition in whole-body PET/CT images. Med. Phys. 43 (1), 613–629.

Well, D.S., Meier, J.M., Mahne, A., Houseni, M., Hernandez-Pampaloni, M., Mong, A., Mishra, S., Zhuge, Y., Souza, A., Udupa, J.K., Alavi, A., Torigian, D.A., 2007. Detection of age-related changes in thoracic structure and function by computed tomography, magnetic resonance imaging, and positron emission tomography. Semin. Nucl. Med. 37, 103–119.

Zhou, J., Rajapakse, J.C., 2005. Segmentation of subcortical brain structures using fuzzy templates. NeuroImage 28, 915–924.

Monica Matsumoto was a post-doctoral researcher in the Medical Image Processing Group, Department of Radiology, University of Pennsylvania from January 2012 till May 2014, developing image analysis methods for Ultrasound and CT images. She obtained her BSc and MSc degrees in Electronic and Computer Engineering in 2005 and 2007, respectively, from the Aeronautics Institute of Technology, and her PhD from the Heart Institute, University of Sao Paulo, Brazil.